Agricultural Water Management 128 (2013) 120–130

Contents lists available at SciVerse ScienceDirect

Agricultural Water Management

journal homepage: www.elsevier.com/locate/agwat

Plot-scale modeling of soil water dynamics and impacts of drought conditions beneath rainfed maize in Eastern Nebraska

Paolo Nasta*, John B. Gates

Department of Earth and Atmospheric Sciences, University of Nebraska-Lincoln, Lincoln, NE, USA

ARTICLE INFO

Article history:
Received 21 December 2012
Accepted 28 June 2013

Keywords:
Rainfed maize
Root water uptake
Soil profile
Water stress
Soil water balance
Climate forcing

ABSTRACT

Intermittent drought periods pose major challenges to the management of rainfed agricultural systems because their productivity is sensitive to water stress during crop development. The objective of this study was to assess soil water dynamics and crop stress patterns during the drought year of 2012, which was among the most severe on record in the US Corn Belt. The study utilized a continuous matric potential profile monitoring record from June 2008–December 2012 beneath a rainfed corn plot in Eastern Nebraska to provide a direct comparison of the 2012 growing season with moderate to relatively wet periods within 2008–2011. The analysis was based on a transient unsaturated zone model that was calibrated with laboratory-measured water retention functions and matric potential measurements from heat dissipation sensors. In each year of the model simulation, soil water storage volumes steadily decreased during the growing season and increased episodically following precipitation events outside of the growing season. Precipitation during the 2012 growing season was <50% of the mean for growing seasons 2009–2012 consequently, soil water storage loss during 2012 was ~14% of initial storage in comparison to 8–9% in 2009–2011. Model results suggest that the 2012 soil water deficit was partially buffered by upward flux of deep soil moisture, with approximately 17% of root water uptake in 2012 deriving from moisture redistributed from below the root zone. Nevertheless, root zone matric potentials exceeded the crop wilting point ($\psi = -8000$ cm) in 2012 for the first time within the monitoring record. These results highlight the need for heightened attention to drought resilience of rainfed cropping systems given future climate predictions that involve increase rainfall intermittency.

1. Introduction

Current and future rates of global food production are highly dependent upon the productivity of rainfed agriculture. As of 2000, approximately 75% of global harvested agricultural area and 66% of total cereal crop production was associated with rainfed agriculture (Portmann et al., 2010). Although typically less productive in terms of crop yield per unit area than irrigated systems (Bruinsma, 2003; Siebert and Döll, 2010), it is likely that rainfed crop production will account for a significant percentage of future gains in global food yields (Rosegrant et al., 2002). One key factor that affects the continued importance of rainfed agriculture is that water supply for large-scale irrigation is likely to become increasingly scarce in many regions. Long-term declines of groundwater storage volumes have been widely documented in many irrigated basins (McGuire, 2009; Scanlon et al., 2012; Aeschbach-Hertig and Gleeson, 2012), and recent estimates have suggested that global groundwater extractions exceed sustainable levels by a factor of two or more on average globally, with much higher values apparent in several major agricultural regions (Wada et al., 2010; Gleeson et al., 2012). Thus, optimizing crop yields of rainfed systems is critical for both meeting future global food security goals and sustaining freshwater resources.

Rainfed production of corn (*Zea mays* L.) in the United States plays an important role in global grain supply given that >50% of global corn exports derive from the US and that approximately 60% of planted corn area in the US is currently managed under rainfed conditions (USDA/NASS; http://www.nass.usda.gov/; last accessed 12 December 2012). Mean annual rainfall generally decreases from east to west across the US Corn Belt, and as a result the spatial distribution of rainfed cultivation is largely centered upon central and eastern areas where seasonal water availability (from residual soil moisture and precipitation during the growing season) is greatest. Although rainfed crop yields per hectare in these areas are often amongst the world's highest (FAOSTAT 2010 data, http://faostat.fao.org; last accessed 12 December 2012; Kucharik and Ramankutty, 2005), yields can be sharply reduced

Abbreviations: RWU, root water uptake; RMSE, root mean squared error; DOY, day of year; GS, growing season; WY, whole year.

* Corresponding author. Tel.: +1 4028906874.
E-mail address: paolo.nasta@unina.it (P. Nasta).

0378-3774/$ – see front matter © 2013 Elsevier B.V. All rights reserved.
http://dx.doi.org/10.1016/j.agwat.2013.06.021

Nomenclature

α	water retention shape parameter, cm^{-1}
a	empirical coefficient in Eq. (5), $cm\,d^{-1}$
b	empirical coefficient in Eq. (5), –
β	transpiration efficiency function, –
D	water drainage, $cm\,d^{-1}$
ε	soil porosity, $cm^3\,cm^{-3}$
E_a	actual evaporation, $cm\,d^{-1}$
E_p	potential evaporation, $cm\,d^{-1}$
ET_0	reference potential evapotranspiration, $cm\,d^{-1}$
ET_c	maize potential evapotranspiration, $cm\,d^{-1}$
H_r	relative humidity, –
K	hydraulic conductivity, $cm\,d^{-1}$
κ	extinction coefficient, –
K_c	crop coefficient, –
K_s	saturated hydraulic conductivity, $cm\,d^{-1}$
LAI	leaf area index, $cm^2\,cm^{-2}$
m	water retention shape parameter, –
n	water retention shape parameter, –
P	gross precipitation, $cm\,d^{-1}$
Q	cumulative water flux, cm
R	net rainfall, $cm\,d^{-1}$
ρ_b	dry bulk density, $g\,cm^{-3}$
RI	rainfall interception, $cm\,d^{-1}$
R_n	net solar radiation, $MJ\,m^{-2}\,d^{-1}$
T	air temperature, °C
τ	tortuosity parameter, –
t	time, d
T_a	actual transpiration, $cm\,d^{-1}$
T_p	potential transpiration, $cm\,d^{-1}$
WS	water storage, cm
W_{sp}	wind speed, $m\,s^{-1}$
ψ	soil matric potential, cm
ψ_{max}	maximum allowed soil matric potential, cm
ψ_{min}	minimum allowed soil matric potential, cm
ψ_{obs}	observed soil matric potential, cm
ψ_{sim}	simulated soil matric potential, cm
ψ_{surf}	surface soil matric potential, cm
z	soil depth, cm
z_r	root zone depth, cm
θ	soil water content, $cm^3\,cm^{-3}$
θ_r	residual water content, $cm^3\,cm^{-3}$
θ_s	saturated water content, $cm^3\,cm^{-3}$

in situations where drought periods coincide with the growing season (Schlenker and Roberts, 2006; Grassini et al., 2009).

In 2012, the Corn Belt region was affected by the most severe drought to affect US agriculture in at least 25 years (USDA/ERS, http://www.ers.usda.gov; National Drought Mitigation Center, http://droughtmonitor.unl.edu, last accessed 12 December 2012). The transition from approximately 50 cm of precipitation in the 2011 growing season to 24 cm of precipitation in the 2012 growing season at the study site (High Plains Regional Climate Center; http://www.hprcc.unl.edu/maps/normals/; last accessed 10 December 2012) offers an excellent opportunity to gauge how soil water dynamics respond to temporal extremes in rainfall. This topic has high relevance for the resilience of rainfed agricultural systems with respect to climatic variability and drought (Rockström et al., 2004; Cooper et al., 2008; Rockström et al., 2009). In particular, recent modeling projections have suggested that future climatic conditions may include increased frequency and severity of extreme weather events (IPCC, 2007). Therefore, field investigations under extremes of moisture availability are desirable in order to gain a better understanding of how soil water and crop yields are affected by rapid climatic variability. Also, in cases where crop yields may strongly benefit from relatively small investments in supplemental irrigation during dry spells, detailed assessment of soil water dynamics can help to refine amounts and timing of water applications (Rockström et al., 2004).

The primary aim of this study was to assess plot-scale soil water dynamics and temporal patterns of crop water stress beneath rainfed corn during the 2012 drought-affected growing season in comparison to previous years (2008–2011). The study utilized near-continuous unsaturated zone profile matric potential monitoring in order to support transient modeling of soil water dynamics within and below the root zone. Monitoring of soil moisture and matric potentials has been widely used to characterize soil water availability beneath rainfed corn on a range of spatial scales (Assouline et al., 2012; Irmak et al., 2012; Li et al., 2012). Development of hydrologic flux estimates from matric potentials (e.g. partitioning the soil water budget into redistribution, drainage, evaporation and transpiration) further requires characterization of hydraulic properties of the vadose zone and crop physiological parameters that affect root water uptake (Feddes et al., 2004; Bastiaanssen et al., 2007). Although many previous studies have investigated soil water dynamics under irrigated corn using transient modeling with the Richards equation (recent examples from this journal include Panda et al., 2004; Chen et al., 2010; Mastrocicco et al., 2010), to our knowledge, this is the first reported modeling of root zone soil water dynamics under rainfed corn production to utilize continuous profile matric potential monitoring with heat dissipation sensors. Also, as a forward unsaturated zone modeling application, the study incorporates an uncommon level of detail in field measurements available for calibration and validation, including multiple years of hourly matric potential measurements at several depths within and below the root zone, local weather data, and layered unsaturated hydraulic properties determined by laboratory measurement (rather than pedotransfer functions, which have a higher degree of uncertainty).

2. Materials and methods

2.1. Study location

The study site is located within a rainfed (non-irrigated) field in Eastern Nebraska (near the town of Oakland, Burt County; 96.53° E, 41.83° N; 415 m a.s.l.) within an area of rolling terrain associated with glacial till and stream dissection of overlying loess units. Mean annual precipitation is about 66 cm/year from 1982 to 2012 (data for December 2012 incomplete at the time of writing), and local monitoring records show significant interannual variability in annual precipitation, ranging between 23 cm in 1983 and 105 cm in 1982 and a variation of approximately 4 °C in average annual temperature, ranging between 7.1 °C in 1996 and 11.5 °C in 2012 (Fig. 1a). Annual precipitation disproportionately occurs in spring and early summer (the wettest months are typically April, May and June; Fig. 1b).

2.2. Field and laboratory measurement methods

Heat dissipation matric potential sensors (model number 229L, Campbell Scientific, Pullman, WA) were installed in a vertical profile in the unsaturated zone on 5 June 2008 (depths 30, 61, 91, 152 and 244 cm). The heat dissipation sensor method was chosen over other widely-used methods, such as field tensiometry, for the combined reasons of (1) measurement range and (2) suitability for long-term monitoring. In contrast to tensiometric measurements, heat dissipation sensors have the distinct advantage of not needing

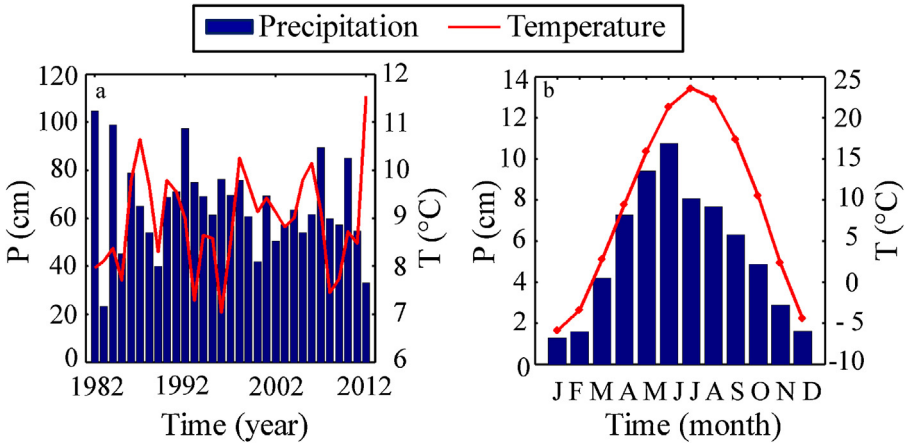

Fig. 1. (a) Annual cumulative precipitation, P (blue bars) and average temperature, T (red line) at the study site (1982–2012) and (b) monthly climate normals (1982–2012).

intermittent refilling or degassing. Moreover, the tensiometric measurement range is typically limited to above ~1000 cm, which is a serious limitation for rainfed agricultural applications because matric potentials during the growing season can reach significantly lower values. The measurement principle of heat dissipation sensors has been described in detail elsewhere (Flint et al., 2002; product manual available at http://www.campbellsci.com) and is briefly summarized here. Each sensor includes a porous ceramic sheath surrounding a heating element. The sensor's rate of temperature increase after an applied heating pulse is sensitive to the pore water content of the ceramic, which in turn is driven by ambient matric potentials. Heat pulse timing and duration is controlled by a data logger, and temperatures are measured with internal thermistors, providing hourly matric potential records. Prior to installation, sensor-specific calibration curves of heat dissipation rates (temperature change over a 20 s interval following a heat pulse) versus matric potentials were determined using a multi-point laboratory calibration procedure using regulated pressure plate chambers following the method of Flint et al. (2002). Field-deployed sensors were surrounded with silica flour to ensure good hydraulic contact with surrounding sediments, and placed at designated depths within an unsaturated zone borehole that was subsequently back-filled with core sediments and then capped to prevent preferential flow.

Undisturbed soil samples were collected at four depths (38 cm, 114 cm, 187 cm, and 267 cm) to measure soil hydraulic and physical properties. Particle-size distribution (PSD) analyses (Gee and Or, 2002) classified the soils from silty clay to silty clay loam (Table 1). Saturated hydraulic conductivity values K_s (cm d^{-1}) were measured by either the constant or the falling head method with four repetitions for each soil sample (Reynolds and Elrick, 2002). The saturated soil water content values θ_s (cm^3 cm^{-3}) and the drying soil water retention data points were measured using a pressure plate apparatus (Dane and Hopmans, 2002). Oven-dried (105 °C) soil cores were used to determine dry bulk density ρ_b (g cm^{-3}), and total porosity ε was calculated from dry bulk density assuming a particle density of 2.65 g cm^{-3} (Table 1).

An automated weather station recorded daily gross precipitation P (cm d^{-1}), air temperature T (°C), relative humidity H_r (%), wind speed W_{sp} (m s^{-1}), and net solar radiation R_n (MJ m^{-2} d^{-1}) (NOAA-NWS, 2007). The reference potential evapotranspiration ET_0 (cm d^{-1}) was computed with the Penman–Monteith equation from the meteorological data (Allen et al., 1998). The crop coefficient (K_c; dimensionless), the leaf area index (LAI; dimensionless) and root growing function for maize were derived from published literature on corn in Nebraska (Sharma and Irmak, 2012; Piccinni et al., 2009). These parameters are specified as a function of time (day of year or DOY) according to growth stage: bare soil for vegetation dormancy from January 1 (DOY 1) to May 9 (DOY 129); crop planting and emergence from May 10 (DOY 130) to July 15 (DOY 196); tassel, silking and blister-kernel phases from July 16 (DOY 197) to August 2 (DOY 214); mature growth phase from August 3 (DOY 215) to October 31 (DOY 305); bare soil for vegetation dormancy from November 1 to December 31 (DOY 306-365). Leap years (2008 and 2012) have an additional day. The code to compute the DOY is reported in Table 2.5 of Allen et al. (1998). The corresponding linear equations are as follows:

$$K_c = \begin{cases} 0.1 & 1 < \text{DOY} < 129 \\ 0.0144\,\text{DOY} - 1.77 & 130 < \text{DOY} < 196 \\ 1.05 & 197 < \text{DOY} < 214 \\ -0.0118\text{DOY} + 3.59 & 215 < \text{DOY} < 305 \\ 0.1 & 306 < \text{DOY} < 365 \end{cases} \quad (1)$$

$$\text{LAI} = \begin{cases} 0 & 1 < \text{DOY} < 129 \\ 0.083\,\text{DOY} - 10.83 & 130 < \text{DOY} < 196 \\ 5.5 & 197 < \text{DOY} < 214 \\ -0.062\,\text{DOY} + 18.79 & 215 < \text{DOY} < 305 \\ 0 & 306 < \text{DOY} < 365 \end{cases} \quad (2)$$

The root depth (z_r) is described by a continuous growing function from DOY 130 ($z_r = 0$) to DOY 305 (maximum $z_r = 135$ cm) with the following equation:

$$z_r = \begin{cases} 0 & 1 < \text{DOY} < 129 \\ 0.776\,\text{DOY} - 100.86 & 130 < \text{DOY} < 305 \\ 0 & 306 < \text{DOY} < 365 \end{cases} \quad (3)$$

Eqs. (1)–(3) do not take into account interannual physiological adaptation of the crop. Potential crop evapotranspiration ET_c (cm d^{-1}) is estimated as ET_0 multiplied by K_c. ET_c is subsequently partitioned into potential evaporation E_p (cm d^{-1}) and potential transpiration T_p (cm d^{-1}) according to the following empirical equation:

$$E_p = ET_c e^{-\kappa\,\text{LAI}} \quad (4)$$

where κ (–) is the dimensionless extinction coefficient for global solar radiation inside the canopy and is assumed to be equal to 0.463 (Ritchie, 1972). The residual fraction of the potential evapotranspiration is assumed equal to the potential transpiration, T_p.

Table 1
Measured physical properties of the soil profile at the monitoring site including textural percentages and classifications, soil bulk density (ρ_b) and soil porosity (ε).

Profile interval, cm	Sample depth, cm	Sand, %	Silt, %	Clay, %	Classification	ρ_b, g cm^3	ε, cm^3 cm^{-3}
0–42	38	3.4	55.1	41.5	Silty clay	1.18	0.556
43–120	114	3.2	60.3	36.5	Silty clay loam	1.21	0.543
121–228	187	3.1	68.7	28.2	Silty clay loam	1.37	0.483
229–300	267	3.0	65.8	31.2	Silty clay loam	1.29	0.514

The rainfall interception RI (cm d^{-1}) is calculated according to Braden (1985):

$$\mathrm{RI} = a\,\mathrm{LAI}\left(1 - \frac{1}{1 + b\,P/a\,\mathrm{LAI}}\right) \tag{5}$$

where a (cm d^{-1}) is an empirical coefficient, assumed as 0.025 cm d^{-1} and b (–) denotes the soil cover fraction given by:

$$b = 1 - e^{-\kappa\,\mathrm{LAI}} \tag{6}$$

Interception is subtracted from the measured rainfall in order to obtain the net rainfall (R). Fig. 2 illustrates the aforementioned water fluxes (P, E_p and T_p) for the same time record associated to the matric potential monitoring.

2.3. Numerical modeling methods

The numerical HYDRUS-1D model (Šimůnek et al., 2008) was used to simulate vertical movement of water in the unsaturated zone and root water uptake (RWU). HYDRUS-1D numerically integrates the following one-dimensional Richards equation:

$$\frac{\partial\theta}{\partial t} = C(\psi)\frac{\partial\psi}{\partial t} = \frac{1}{\partial z}\partial\left[K(\psi)\left(\frac{\partial\psi}{\partial z} + 1\right)\right] - \xi(\psi) \tag{7}$$

where t (d) is time, z (cm) is soil depth (positive upward), θ (cm^3 cm^{-3}) is the soil volumetric water content, $C(\psi)$ is the differential water capacity function (cm^{-1}), and $\xi(\psi)$ is the RWU sink term (d^{-1}). Osmotic potentials are assumed to be negligible because of the low soil water salinity at the site. The soil water retention function $\theta(\psi)$ is described by van Genuchten's equation (van Genuchten, 1980):

$$\theta(\psi) = \theta_r + \frac{\theta_s - \theta_r}{\left[1 + (\alpha\psi)^n\right]^m} \tag{8a}$$

with Mualem's condition (Mualem, 1976):

$$m = 1 - \frac{1}{n} \tag{8b}$$

where α (cm^{-1}), m (–) and n (–) are shape parameters, θ_r (cm^3 cm^{-3}) and θ_s (cm^3 cm^{-3}) are residual and saturated water contents, respectively. Considering the degree of saturation, $S_e = (\theta - \theta_r)/(\theta_s - \theta_r)$, which varies from 0 ($\theta = \theta_r$) to 1 ($\theta = \theta_s$), an expression for the unsaturated hydraulic conductivity function $K(S_e)$ is obtained by combining Eq. (8a) with the pore-size distribution model of Mualem (1976) to yield:

$$K(S_e) = K_s S_e^{\tau}\left[1 - \{1 - S_e^{1/m}\}^m\right]^2 \tag{9}$$

where τ (–) represents the tortuosity parameter. Tortuosity is commonly assumed to be either $\tau = 0.5$ (Mualem, 1976), $\tau = 2$ (Burdine, 1953), $\tau = -1$ (Schaap and Leij, 2000), or is calculated from simultaneous water retention and conductivity measurements. In this study, the water retention parameters (α, n, θ_r and θ_s) retrieved from the direct measurements are inserted in Eq. (9) and τ is estimated as a fitting parameter in the hydraulic conductivity function. Increasing values of τ have the effect of decreasing the term S_e^{τ} in Eq. (9) and therefore decreasing the hydraulic conductivity function $K(S_e)$ such that it will vary from 0 ($S_e = 0$) to K_s ($S_e = 1$).

The soil profile lower boundary is 300 cm depth and the profile is subdivided into four soil layers (assumed internally homogeneous) according to textural and hydraulic information (0–42 cm, 43–120 cm, 121–228 cm, 229–300 cm). For each soil layer, θ_s and K_s were measured (see description above), whereas the remaining soil hydraulic parameters (θ_r, α and n) were obtained by fitting Eq. (8) to the measured retention data and minimizing the squared prediction errors (as shown in Fig. 3 and summarized in Table 2). The RWU sink term ξ (Eq. (7)) is defined as:

$$\xi(\psi) = \beta(\psi)\varphi(z_r)T_p \tag{10}$$

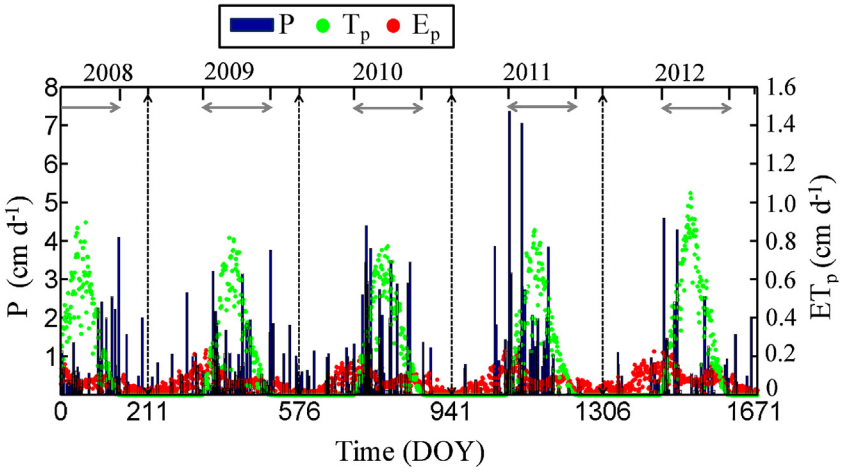

Fig. 2. Daily values of precipitation (P), potential evaporation (E_p), and potential transpiration (T_p) for the time record June 2008–December 2012. Snowfall is not reported. Vertical dashed lines denote calendar years (1 < DOY < 365) and horizontal arrows denote the growing seasons (130 < DOY < 305).

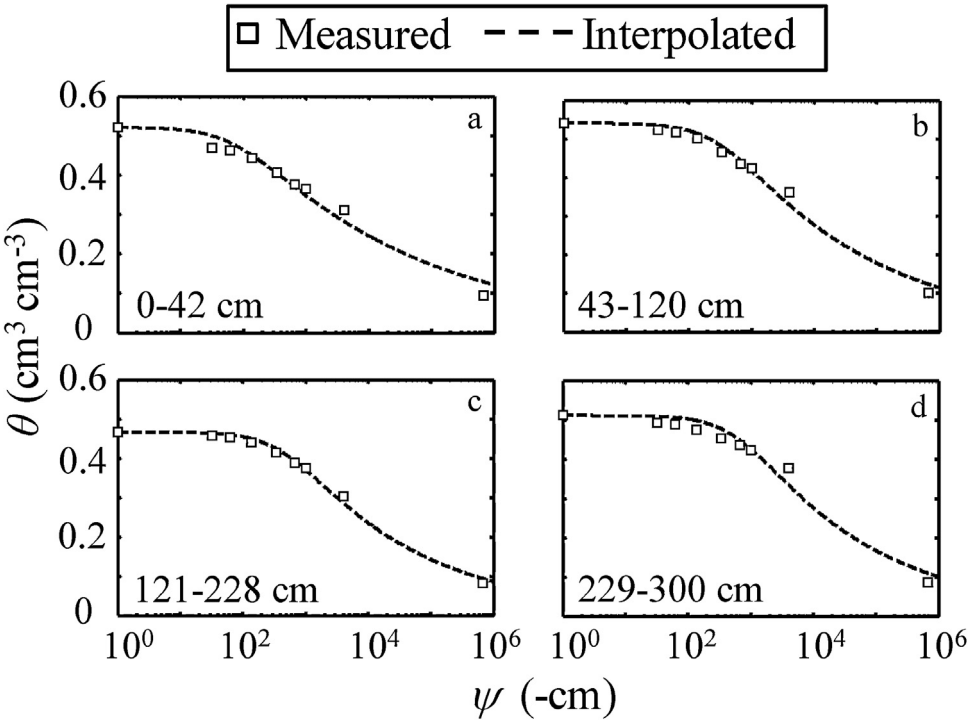

Fig. 3. Measured (points) and optimized (dashed lines) water retention functions for (a) 0–42 cm depth; (b) 43–120 cm depth; (c) 121–228 cm depth; and (d) 229–300 cm depth.

where $\varphi(z_r)$ (cm^{-1}) is the normalized water uptake distribution and $\beta(\psi)$ is the dimensionless RWU efficiency function ($0<\beta<1$), which depends on the soil matric potential and determines water stress. The root density distribution of corn was assumed to linearly decrease with increasing soil depth (Feddes et al., 1978). The RWU stress parameters for maize were specified using literature-derived values that are integrated as default values into the HYDRUS-1D software package (Šimůnek et al., 2008). Optimal root water extraction ($\beta=1$) occurs within the matric potential range $-30\,cm>\psi>-600\,cm$. Water stress ($0<\beta<1$) then decreases linearly up to the estimated wilting point for corn ($\psi=-8000\,cm$) for which there is total reduction ($\beta=0$) (Coelho and Or, 1999; Metselaar and de Jong van Lier, 2007). The actual transpiration flux, equivalent to root water extraction rate T_a ($cm\,d^{-1}$) integrated across the root zone, was computed by numerical integration of Eq. (10).

The system-dependent upper boundary conditions are daily net precipitation ($R=P-RI$) and potential evaporation (E_p). Freezing and thawing of precipitation is assumed to occur instantaneously according to mean daily temperature. The minimum allowable soil matric potential value at the upper boundary (ψ_{min}; denoted "*hCritA*" in HYDRUS-1D) was calculated through the Kelvin equation:

$$\psi_{min}=-\frac{G_c T}{Mg}\ln\ H_r \qquad (11)$$

where M is the molecular weight of water (=0.018015 $kg\,mol^{-1}$), g is the gravitational acceleration constant (=981 $cm\,s^{-2}$) and G_c is the gas constant (=8.314 $J\,mol^{-1}\,K^{-1}$). When surface matric potential ψ_{surf} is less than ψ_{min}, the prescribed flux on the upper boundary of the soil profile switches to a constant head type boundary condition (Dirichlet's condition), resulting in reduction of the potential evaporation (E_p) into actual evaporation (E_a). A proportion of R is routed into runoff if ψ_{surf} exceeds the maximum soil surface matric potential value $\psi_{max}=0.5\,cm$ that represents the nominal depth of surface water ponding allowable before runoff generation.

Free drainage is assumed at the bottom boundary of the soil profile domain (300 cm), enabling continuous (downward) drainage to occur under a unit total hydraulic gradient (driven by only the gravitational gradient component). Initial conditions were specified by linearly interpolating measured matric potentials corresponding to the initial time (first DOY, 5 June 2008). The simulations were undertaken using a finite element grid with finer spacing at the top of the soil profile (0.55 cm) and coarsening with depth (5.46 cm grid at 300 cm depth).

2.4. Model calibration methods

Calibration was achieved by adjusting the tortuosity parameter (τ_j) for each soil layer j to optimize model fit to measured soil matric potentials during 2008. The τ_j-values were assigned by minimizing the squared errors between observed (ψ_{obs}) and simulated (ψ_{sim}) soil matric potential values with the Levenberg–Marquardt nonlinear minimization method (Marquadt, 1963). The objective function OF(ϕ) embeds the vector ϕ that includes the four

Table 2
Hydraulic parameters of the soil profile: residual water content (θ_r), saturated water content (θ_s), shape parameters (α and n) and saturated hydraulic conductivity (K_s).

Profile interval, cm	Sample depth, cm	θ_r, $cm^3\,cm^{-3}$	θ_s, $cm^3\,cm^{-3}$	α, cm^{-1}	n, –	K_s, $cm\,d^{-1}$
0–42	38	0.095	0.521	0.0129	1.15	181.47
43–120	114	0.101	0.541	0.0031	1.19	9.53
121–228	187	0.081	0.467	0.0022	1.22	1.65
229–300	267	0.085	0.511	0.0153	1.18	0.81

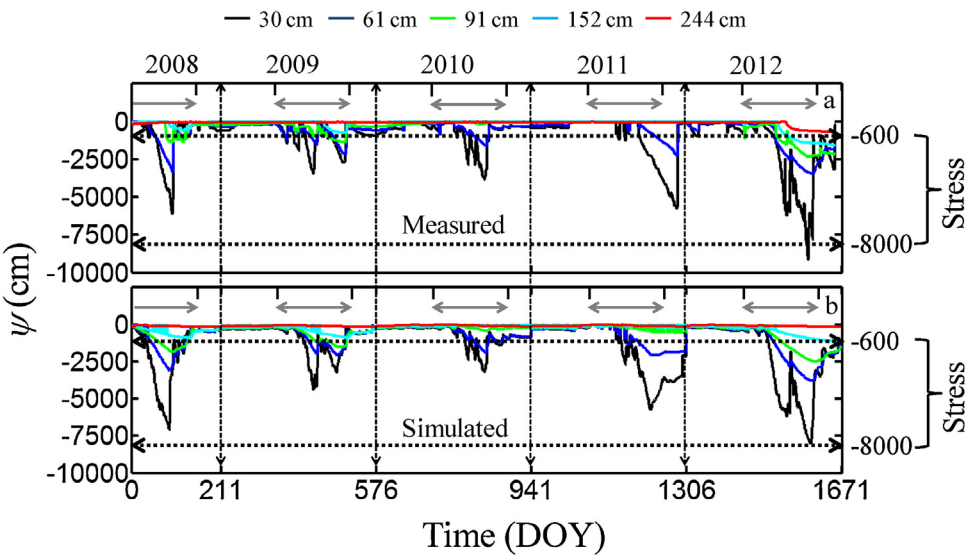

Fig. 4. (a) Measured and (b) simulated soil matric potential (ψ) values for the monitored soil depths during the calibration (2008) and validation (2009–2012) periods. Matric potential ranges associated with root water uptake stress are also shown. Horizontal arrows denote the growing seasons (130 < DOY < 305).

tortuosity parameters τ_j for each soil layer j. The OF(ϕ) is defined as:

$$\mathrm{OF}(\phi) = \sum_{i=1}^{N_{08}} \left[\psi_{obs}(t_i) - \psi_{sim}(t_i, \phi)\right]^2 \quad (12)$$

where t_i corresponds to the time (DOY) associated with observed and simulated variables, starting from the first day of the installation (5 June 2008) and ending on 31 December 2008 (N = 210). In order to ensure physical consistency across τ_j values (a fundamental requirement to obtain a monotonically decreasing hydraulic conductivity function), the parameters τ_j were constrained using a minimum value of $-2/m_j < \tau_j$ (Peters et al., 2011). There is no theoretical maximum value for τ_j; however, previous studies suggest that τ_j usually does not exceed the value of 15 (Schuh and Cline, 1990; Kosugi et al., 2002). Because the objective function may be strongly affected by local minima during the search, the inversion procedure was iteratively executed using varying combinations of initial estimates.

Quantitative model performance was assessed using the root mean squared errors (RMSE) between daily measured and modeled matric potentials, expressed in $\log_{10}$-scale:

$$\mathrm{RMSE} = \sqrt{\frac{\sum_{i=1}^{N}\left[\log_{10}\psi_{obs}(t_i) - \log_{10}\psi_{sim}(t_i)\right]^2}{N}} \quad (13)$$

where N is the number of days. Three RMSE types are presented in Table 4: (1) calibration period ranging from 5 June 2008 up to 31 December 2008 ($\mathrm{RMSE_{cal}}$; N = 210), (2) the entire 2009–2012 post-calibration monitoring record ($\mathrm{RMSE_{val}}$; N = 1448), (3) 2009–2012 measurements that took place during the growing seasons only ($\mathrm{RMSE_{gs}}$; N = 700).

3. Results and discussion

3.1. Measured matric potentials

The measured matric potential record illustrates strong seasonality in soil water conditions throughout each year of the record (2008–2012; Fig. 4a). Rapid drying trends for the shallowest two sensors (30 cm and 61 cm) generally began in May to early June, coinciding with initial crop growth. Increasing time lags relative to the date of drying onset at 30 cm occurred with increasing sensor depth, reflecting the progressive downward propagation of drying fronts each summer. The degree of temporal variability also decreased with depth, and the deepest sensor (244 cm) remained relatively constant throughout the record ($\psi \sim 50$ cm). The local water table is approximately ~300 cm below surface, and it is apparent that the 244 cm sensor remained near saturation because it was within the capillary fringe throughout the monitoring period. The number of sensors reporting matric potentials that are indicative of crop water stress ($\psi < -600$ cm) varied by year. In 2010 and 2011, only the 30 cm and 61 cm sensors fell below $\psi < -600$ cm during the growing season. The 91 cm sensor fell below $\psi < -600$ cm in 2008, 2009 and 2012. The 152 cm sensor only fell below $\psi < -600$ cm during 2012. Yearly minimum matric potentials reported by the 30 cm sensor (shallowest sensor) ranged from $\psi = -3456$ cm in 2009 to $\psi = -9136$ cm in 2012. Winter matric potentials returned to $\psi > -600$ cm for all sensors in all years except for 2012, reflecting weak soil moisture replenishment following the 2012 growing season because of prolonged drought conditions.

3.2. Model calibration and performance

The tortuosity values estimated by statistical fit during the calibration procedure ranged from −1.56 to +5.01. The largest

Table 3
Tortuosity parameters (τ_1, τ_2, τ_3, τ_4) optimized through inverse modeling, including 95% confidence limits and correlation coefficients.

	Depth, cm	τ_{opt}, –	P_{min}, 5%	P_{max}, 95%	τ_1, –	τ_2, –	τ_3, –	τ_4, –
τ_1	38	−1.56	−1.81	−1.31	1			
τ_2	114	−0.0137	−0.26	0.23	0.056	1		
τ_3	187	3.91	2.68	5.14	0.53	0.17	1	
τ_4	267	5.01	−0.028	10.1	0.058	0.13	0.07	1

Table 4
Root mean square errors for the calibration ($RMSE_{cal}$) and validation periods ($RMSE_{val}$ and $RMSE_{gs}$) for each matric potential sensor located in the root zone (z_r) or below the root zone ($z - z_r$). Validation period RMSE-values, $RMSE_{val}$ and $RMSE_{gs}$ are reported both for the whole year (WY) and for the growing season (GS), respectively.

	Sensor depth, cm	$RMSE_{cal}$	$RMSE_{val}$ (WY)	$RMSE_{gs}$ (GS)
z_r	30	0.42	0.49	0.41
	61	0.57	0.52	0.47
	91	0.40	0.82	0.69
$z - z_r$	152	0.84	0.92	0.94
	244	0.40	0.33	0.39

tortuosity values were estimated for the deepest profile layers (Table 3). This pattern is not correlated with sediment texture, and may be partially attributable to soil compaction with depth. However, the large range in the 95% confidence interval for the two deepest layers ($2.68 < \tau_3 < 5.14$ and $-0.03 < \tau_4 < 10.03$) indicates a relatively high degree of uncertainty. Especially for the deepest sensor, the low sensitivity is due to the small temporal variations of the matric potential values that are near saturation. This implies strong equifinality of the tortuosity estimate for the 244 cm sensor because the S_e^{τ} term is close to unity. On the other hand, the very low values of the correlation matrix indicate low inter-dependence of the four tortuosity parameters.

The temporal trends in simulated matric potentials generally agreed well with the observed matric potentials throughout the 2008–2012 monitoring period (Fig. 4a and b). Simulated matric potentials tended to capture both the timing and magnitude of drying patterns in most cases, including the severe drying in 2012. One notable exception was the behavior of the 30 cm and 61 cm sensors during the 2011 growing season; the model predicted a stabilization of matric potentials at approximately DOY 1220 while measured matric potentials continued to sharply decline.

The $RMSE_{cal}$ values for sensors within the root zone range from 0.40 cm to 0.57 cm. $RMSE_{val}$ values were generally comparable to $RMSE_{cal}$ values, suggesting that model performance did not diminish significantly outside of the calibration period. The highest $RMSE_{cal}$ value was for the sensor at 152 cm depth ($RMSE_{cal} = 0.84$ cm), which remained relatively wet throughout the monitoring period and was slightly but consistently underpredicted by the model. The $RMSE_{cal}$ value for the 152 cm sensor was greater than the $RMSE_{cal}$ value for the 244 cm sensor because the former was subject to greater temporal variability.

Cross-comparisons between measured and modeled data primarily cluster along the 1:1 line for $\psi < -100$ cm (Fig. 5a and c), illustrating the strong model performance under relatively dry conditions (which occurred primarily during the growing season). In contrast, divergence from the 1:1 line above $\psi = -100$ cm suggests a systematic model underestimation of simulated matric potential values at higher (wetter) ranges. This bias within the wet range of sensor measurements may be primarily attributable to sensor error, considering that heat dissipation sensors have shown to have reduced performance above $\psi = -100$ cm (Flint et al., 2002). Model structure during crop dormancy periods may also play a role in the wet range bias because K_c during dormancy is poorly constrained (assumed equal to 0.1 in this case, see Eq. (1)) and this period coincided with the wettest near-surface moisture conditions. The distribution of the errors (in decimal logarithmic scale) shows significant negative bias for the full year data set (Fig. 5b), reflecting model underestimation of measured matric potential in the wet range. However, within the growing season, error distributions are approximately Gaussian (according to the χ^2-test; Fig. 5d) without significant over or underestimation. Hence, the model performance is strongest for evaluation of soil water dynamics within the growing seasons under primarily low moisture conditions, which is the focus on this investigation. The fact that $RMSE_{gs}$ values within the root were uniformly lower than $RMSE_{val}$

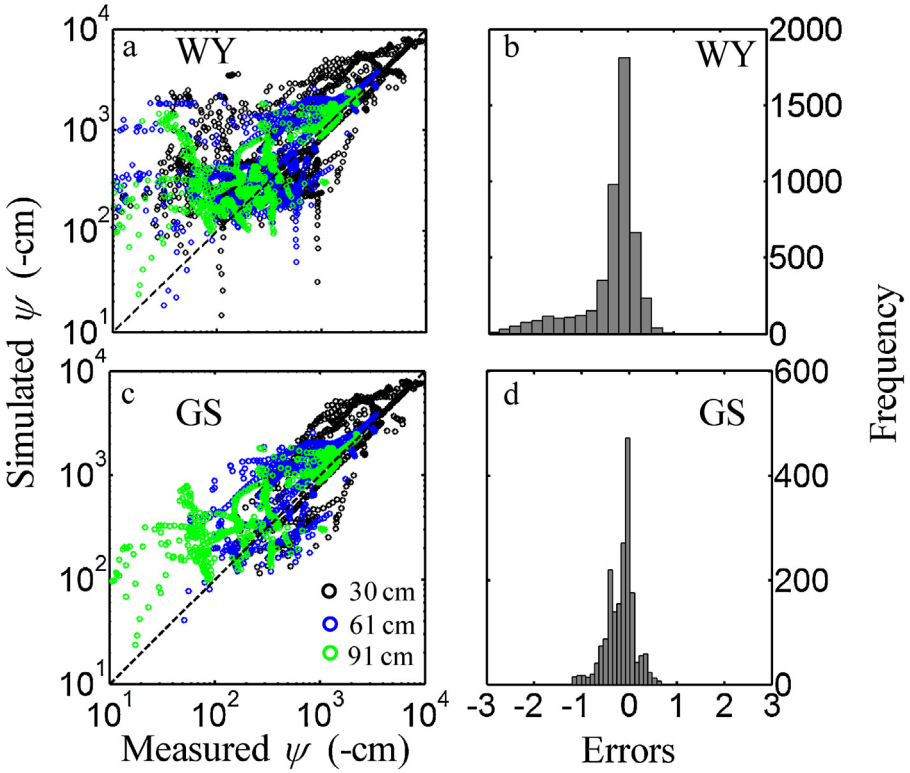

Fig. 5. Error analyses of simulated versus measured matric potentials (in decimal logarithmic scale): (a) scatterplot considering whole year data (WY), (b) frequency distribution of errors considering whole year data (WY), (c) scatterplot considering growing season data only (GS), (d) frequency distribution of errors considering growing season data only (GS). Dashed line in parts (a) and (c) denotes the line 1:1 correlation.

Table 5
Simulated cumulative water fluxes for the growing seasons of 2009–2012: gross precipitation (P), rainfall interception (RI), reference potential evapotranspiration (ET_0), potential crop evapotranspiration (ET_c), potential transpiration (T_p), potential evaporation (E_p), water storage (WS), water drainage (D), actual evaporation (E_a), actual transpiration (T_a) and water stress ($T_p - T_a$).

		2009	2010	2011	2012
Input, cm	P	43.15	62.24	53.71	29.11
	RI	4.64	4.42	3.97	2.22
	ET_0	90.62	100.59	96.53	120.83
	ET_c	60.23	64.42	62.01	79.02
	T_p	48.57	51.57	49.87	63.58
	E_p	11.66	12.85	12.14	15.44
Output, cm	WS_{130}	140.12	141.33	140.55	132.60
	WS_{304}	127.77	130.29	127.29	114.34
	D	−0.71	−5.22	−5.38	−0.48
	E_a	11.60	12.80	12.03	15.14
	T_a	38.91	45.91	45.07	29.55
	Stress ($T_p - T_a$)	9.66	5.66	4.80	34.03

confirms that model performance is most precise during the growing season.

3.3. Water budget

Precipitation amounts during the growing seasons 2009–2012 ranged from a maximum of 62 cm in 2010 to a minimum of 29 cm in 2012 (Table 5). Although 2012 had the lowest annual amount of growing season precipitation within the 2008–2012 period, a similarly low rainfall total occurred in the 1983 growing season according to local meteorological records (see Fig. 1a). Simulated rainfall interception (RI) rates were approximately 10% of gross precipitation (P) for each growing season 2008–2012. Simulated growing season ET_c values were similar for 2009, 2010 and 2011 (range of approximately 60–64 cm); 2012 had a higher value of 79 cm (the reduction of ET_0 into ET_c associated with K_c was approximately 35% for all four years). E_p represented approximately 20% of ET_c based on Eq. (4). Typical of local climatic conditions, E_p and T_p portrayed relatively regular periodic patterns, whereas precipitation had greater temporal variability and episodicity. Simulated runoff was negligible because water potentials at the soil surface rarely exceeded ψ_{max}. Also, reductions of E_a relative to E_p tended to be small (i.e. $E_a \approx E_p$) because water potentials at the soil surface were rarely lower than ψ_{min}.

Modeled soil water fluxes and storage trends are synthesized in Table 5 and Fig. 6. Soil water storage volumes decreased each year during the growing season. The amount of soil water storage loss during the growing season was relatively constant at approximately 12 cm per season in 2009–2011 (Table 5; WS_{130} and WS_{305} indicate soil water storage at the initial and final days of growing season, respectively). As a percentage of total root zone water storage at the beginning of the growing season, water storage losses were 8.8%, 7.8% and 9.4% for the growing seasons of 2009, 2010, and 2011, respectively. In contrast, soil water storage loss during the 2012 growing season was approximately 18 cm, or 13.8% of initial storage, reflecting the significantly lower growing season precipitation total (29 cm compared to 62 cm in 2010, for example). Water loss attributable solely to evapotranspiration can be assessed by subtracting water loss from deep drainage (D) from the storage changes over the growing season. Considering that the deep drainage in the growing seasons of 2010 and 2011 was approximately 5–6 cm per season, it may be inferred that water loss attributable to evapotranspiration in 2009 was about twice that of 2010 and 2011. The soil water loss attributable to evapotranspiration in the drought event of 2012 was greater than those observed in the relatively wet years of the record (2010 and 2011) by a factor of approximately four. After each growing season, soil water storage increased intermittently following precipitation events in fall

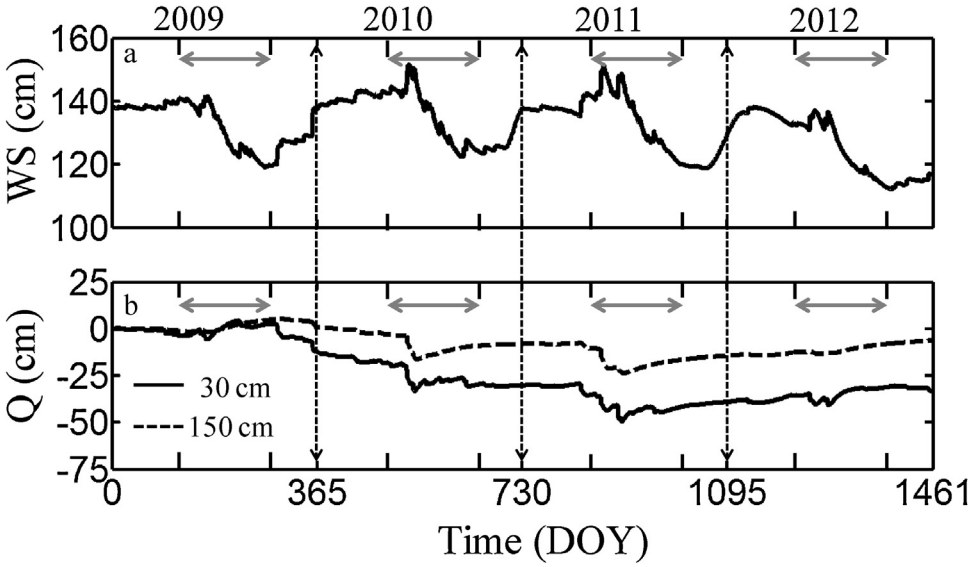

Fig. 6. Simulated cumulative water budget terms for 2009–2012: (a) water storage (WS; cm) and (b) water fluxes (Q) at 30 cm depth (solid line) and at 150 cm depth (dashed line). Horizontal arrows delimit the growing season (130 < DOY < 305).

and snowmelt and storm events in spring (Fig. 6a). Both the timing and the peak soil water storage amounts were relatively consistent across each year of the monitoring record, occurring during the spring and reaching maximum storage values of 141–153 cm.

In 2009–2011, water redistribution within the root zone was predominantly downward (negative) outside of the growing season based on simulated water fluxes at 30 cm (Q_{30}) and 150 cm soil depth (Q_{150}) (Fig. 6b). Flow directions tended to be reversed in each growing season, during which upward moisture flow was driven by near-surface evapotranspiration. The 2012 growing season featured a notable decrease of matric potential values for all sensors except the 244 cm, which was affected by the capillary fringe. Simulated fluxes across the root zone boundary (approximated by Q_{150}) suggest that deep (sub-root zone) soil moisture tended to function as a water source to the root zone during the growing seasons, whereas negative values indicate that deep drainage occurs in the wet seasons (Fig. 6b). Comparison of annual Q_{150} values with T_a values suggest that deep soil moisture contributions accounted for 0–17% of annual root water uptake (17% in 2009 and 2012; negligible contributions in 2010 and 2011). Simulated cumulative lower boundary drainage rates (across the 300 cm depth plane) were less than 1 cm in the growing seasons of 2009 and 2012, and approximately 5–6 cm for 2010 and 2011 (Table 5), with most drainage events in 2010 and 2011 occurring during late spring when the soil water storage is near its maximum. However, the assumed free drainage lower boundary condition does not permit positive values for deep drainage. Therefore, possible discharges from the water table could not be assessed.

3.4. Crop water stress

Seasonal evolution of plant water stress is evaluated using simulated $T_p - T_a$ as an indicator of root water uptake reduction (shown in Fig. 7). Results suggest that RWU stress was intermittent within each growing season throughout the monitoring period, and in some cases shifted rapidly after weather events. For example, water stress sharply declined in 15 August 2009 (from 0.311 to 0.018 cm d^{-1} on consecutive days) following a 2.16 cm rainfall event. A similar scenario occurred between August 21 and August 22 in 2011. Maximum water stress occurred with similar timing (early to mid-August) in each of the monitoring years. The simulated soil matric potential corresponding to shallowest depth fell below the wilting point ($\psi = -8000$ cm) in 2012 for the first time within the monitoring period. Significant inter-annual variability in cumulative water stress was also evident (Table 5). Cumulative growing season water stress ranged from a minimum of 5 cm to a maximum of 9 cm per season in 2009–2011, compared to 34 cm in 2012 (Table 5; Fig. 7). On a percentage basis, reductions

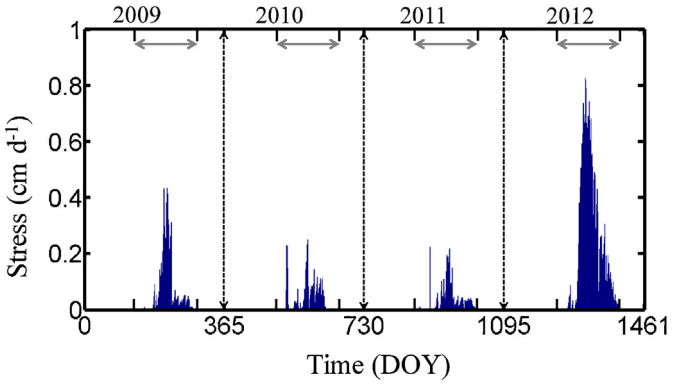

Fig. 7. Simulated crop water stress defined by $T_p - T_a$ (2009–2012). Horizontal arrows delimit the growing season (130 < DOY < 305).

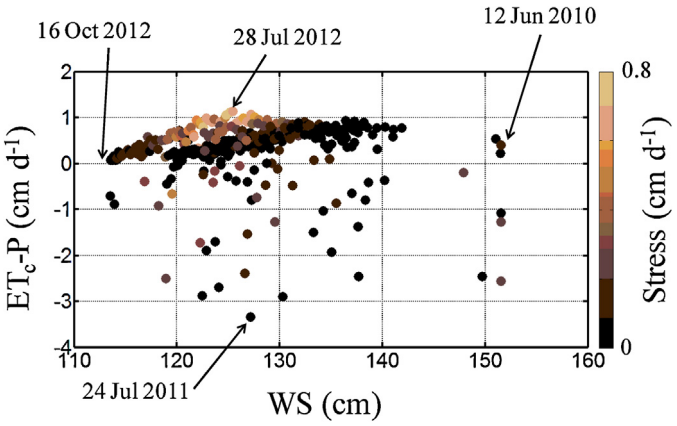

Fig. 8. Crop water stress (shown with degree of shading) as a function of daily climatic boundary conditions ($ET_c - P$) and soil water storage (WS) 2009–2012.

in transpiration due to water stress equated to a mean of 14% of T_p for 2009–2011 and 53% of T_p in 2012. This range strongly contrasts with typical irrigated conditions. For example, Li et al. (2012) observed that reductions in transpiration due to water stress were never less than 20% for maize under irrigated conditions in the Heihe Basin in western China.

Fig. 8 shows the distribution of simulated water stress as a function of climatic ($ET_c - P$) and soil water storage controls. Most daily climatic values fell within the relatively narrow range of 0–1 cm d^{-1}. The small percentage of points with $ET_c - P < 0$ are associated with major rainfall events that led to daily P exceeding ET_c. The most severe daily water stress occurrences were tightly clustered near $ET_c - P = 1$ cm d^{-1} and intermediate water storage values of 120–130 cm. These occurrences of maximum daily water stress mainly coincided with early to middle growing season periods that experienced low rainfall; these were periods when daily $ET_c - P$ values were greatest but soil moisture storage amounts had not yet reached their minimum values (see for example 28 July 2012; Fig. 8). Many of the days with lowest water storage amounts (110–120 cm) did not coincide with high water stress because they occurred soon after the growing season when ET_c was low but water storage had not yet recovered (see for example 16 October 2012; Fig. 8). These results show that crop water stress is more closely related to daily climatic conditions than total water storage in current study area in the Eastern Great Plains. Because few studies have examined the relationships between crop water stress and unsaturated zone dynamics beneath dryland corn, it is unclear how these patterns may vary in different textural, climatic and vegetation conditions. For example, it seems likely that a coarse-textured soil profile with a deeper water table under similar climatic and vegetation conditions would certainly exhibit a closer relationship between crop water stress and profile water storage. Additional research across diverse environmental settings are necessary in order to refine current understanding of how terrestrial factors affect drought impacts on rainfed crop stress.

4. Conclusions

The 2012 drought in the US Corn Belt strongly affected water dynamics in the silty clay to silty clay loam soil profile at the study site in Eastern Nebraska in several respects relative to previous years. Notable effects of the 2012 drought included (1) increasing the seasonal soil water storage depletion rate, (2) lowering near-surface matric potentials to a minimum value that was below the wilting point for corn for the first time in the five year monitoring record (2008–2012), (3) increasing the magnitude of upward water potential gradients, and (4) increasing the contribution of

sub-root zone soil moisture storage to RWU (although on a percentage basis it was comparable to 2009). Resulting water stress-related reductions in transpiration were 55% of potential transpiration in 2012 compared to a mean of 15% for 2009–2011. Results suggest that residual soil water within and below the root zone helped to mitigate harmful crop stress somewhat but was not sufficient to prevent it, and that the most significant periods of crop water stress were most closely associated with dry atmospheric conditions rather than a dry soil profile.

Performance testing of the calibrated one-dimensional numerical flow model suggested that the model's reproduction of observed matric potentials was acceptable and was most precise for the dry range of the record ($\psi < -10^2$ cm). Improvements to the current model's performance could be enhanced with increased realism in crop-related boundary conditions parameters.

Acknowledgments

The authors acknowledge the financial support of the Eastern Nebraska Water Resources Assessment Project (ENWRA) and its sponsor organizations. Field and laboratory data were provided by the US Geol. Surv. Nebraska Water Science Center. Dana Divine and Gregory Steele provided valuable suggestions for the manuscript.

References

Aeschbach-Hertig, W., Gleeson, T., 2012. Regional strategies for the accelerating global problem of groundwater depletion. Nature Geoscience 5 (12), 853–861.

Allen, R.G., Pereira, L.S., Raes, D., Smith, M., 1998. Crop evapotranspiration: guidelines for computing crop water requirements. Irrigation and Drainage Paper No. 56. Food and Agriculture Organization of the United Nations (FAO), Rome, Italy, 300 p.

Assouline, S., Möller, M., Furman, A., Narkis, K., Silber, A., 2012. Impact of water regime and growing conditions on soil–plant interactions: from single plant to field scale. Vadose Zone Journal 1, 1, http://dx.doi.org/10.2136/vzj2012.0006.

Bastiaanssen, W.G.M., Allen, R.G., Droogers, P., D'Urso, G., Steduto, P., 2007. Twenty-five years modeling irrigated and drained soils: state of the art. Agricultural Water Management 92 (3), 111–125.

Braden, H., 1985. Ein Energiehaushalts- und Verdunstungsmodell for Wasser und Stoffhaushaltsuntersuchungen landwirtschaftlich genutzer Einzugsgebiete. Mittelungen Deutsche Bodenkundliche Geselschaft 42, 294–299.

Bruinsma, J. (Ed.), 2003. World Agriculture: Towards 2015/2030 An FAO Perspective. FAO, Earthscan publications Ltd., London.

Burdine, N.T., 1953. Relative permeability calculations from pore-size distribution data. Transactions of the American Institute of Mining and Metallurgical Engineers 198, 71–78.

Chen, C., Wang, E., Yu, Q., 2010. Modelling the effects of climate variability and water management on crop water productivity and water balance in the North China Plain. Agricultural Water Management 97, 1175–1184.

Coelho, E.F., Or, D., 1999. Root distribution and water uptake patterns of corn under surface and subsurface drip irrigation. Plant Soil 206, 123–136, http://dx.doi.org/10.1023/A:1004325219804.

Cooper, P.J.M., Dimes, J., Rao, K.P.C., Shapiro, B., Shiferaw, B., Twomlow, S., 2008. Coping better with current climatic variability in the rain-fed farming systems of sub-Saharan Africa: an essential first step in adapting to future climate change? Agriculture, Ecosystems & Environment 126 (1–2), 24–35.

Dane, J.H., Hopmans, J.W., 2002. Pressure plate extractor. In: Dane, J.H., Topp, G.C. (Eds.), Methods of Soil Analysis: Part 4, Physical Methods. SSSA Book Series No. 5. Soil Science Society of America, Madison, WI, pp. 688–690.

Feddes, R.A., Kowalik, P.J., Zarandny, H., 1978. Simulation of Field Water Use and Crop Yield. John Wiley & Sons, New York, NY.

Feddes, R.A., de Rooij, G.H., van Dam, J.C., 2004a. Unsaturated Zone Modeling, Progress, Challenges and Applications. Wageningen UR Frontis Series, vol. 6. Kluwer Academic Publishers, pp. 364, ISBN: 1-4020-2918-7(PB) www.wur.nl/frontis

Flint, A.L., Campbell, G.S., Ellet, K.M., Calissendorff, C., 2002. Calibration and temperature correction of heat dissipation matric potential sensors. Soil Science Society of America Journal 66, 1439–1445.

Gee, G.W., Or, D., 2002. Particle-size analysis. In: Dane, J.H., Topp, G.C. (Eds.), Methods of Soil Analysis: Part 4, Physical Methods. SSSA Book Series No. 5. Soil Science Society of America, Madison, WI, pp. 255–293.

Gleeson, T., Wada, Y., Bierkens, M.F.P., van Beek, L.P.H., 2012. Water balance of global aquifers revealed by groundwater footprint. Nature 488 (7410), 197–200.

Grassini, P., Yang, H., Cassman, K.G., 2009. Limits to maize productivity in Western Corn-Belt: a simulation analysis for fully irrigated and rainfed conditions. Agricultural and Forest Meteorology 149 (8), 1254–1265.

IPCC, 2007. Climate change 2007: the physical science basis. In: Solomon, S., Qin, D., Manning, M., Chen, Z., Marquis, M., Averyt, K.B., Tignor, M., Miller, H.L. (Eds.), Contribution of Working Group I to the Fourth Assessment Report of the Intergovernmental Panel on Climate Change. Cambridge University Press, Cambridge, UK/New York, NY, USA, 996 pp.

Irmak, S., Burgert, M.J., Yang, H.S., Cassman, K.G., Walters, D.T., Rathje, W.R., Payero, J.O., Grassini, P., Kuzila, M.S., Brunkhorst, K.J., van DeWalle, B., Rees, J.M., Kranz, W.L., Eisenhauer, D.E., Shapiro, C.A., Zoubek, G.L., Teichmeier, G.J., 2012. Large-scale on-farm implementation of soil-moisture-based irrigation management strategies for increasing maize water productivity. Transactions of ASABE 55, 881–894.

Kosugi, K., Hopmans, J.W., Dane, J.H., 2002. Parametric models. In: Dane, J.H., Topp, G.C. (Eds.), Methods of Soil Analysis, Part 4, SSSA Book Ser. vol. 5. SSSA, Madison, Wisconsin, pp. 739–757.

Kucharik, C.J., Ramankutty, N., 2005. Trends and variability in U.S. corn yields over the twentieth century. Earth Interactions 9 (1), 1–29.

Li, Y., Kinzelbach, W., Zhou, J., Cheng, G.D., Li, X., 2012. Modelling irrigated maize with a combination of coupled-model simulation and uncertainty analysis, in the northwest of China. Hydrology and Earth System Sciences 16, 1465–1480.

Marquadt, D.W., 1963. An algorithm for least-squares estimation of nonlinear parameters. SIAM Journal of Applied Mathematics 11, 431–441.

Mastrocicco, M., Colombani, N., Salemi, E., Castaldelli, G., 2010. Numerical assessment of effective evapotranspiration from maize plots to estimate groundwater recharge in lowlands. Agricultural Water Management 97, 1389–1398.

McGuire, V. L., 2009. Water-Level Changes in the High Plains Aquifer, Predevelopment to 2007. 2005–06, and 2006–07. U.S. Geological Survey Scientific Investigations Report 2009-5019, p. 9.

Metselaar, K., de Jong van Lier, Q., 2007. The shape of the transpiration reduction function under plant water stress. Vadose Zone Journal 6, 124–139.

Mualem, Y., 1976. A new model for predicting the hydraulic conductivity of unsaturated porous media. Water Resources Research 12, 513–522.

NOAA-NWS, 2007. Manual 10-1315. Cooperative Station Observations. Surface Observing Program (Land). Operation and Services (online WWW), Available URL: http://www.nws.noaa.gov/directives/sym/pd01013015curr.pdf

Panda, R.K., Behera, S.K., Kashyap, P.S., 2004. Effective management of irrigation water for maize under stressed conditions. Agricultural Water Management 66, 181–203.

Peters, A., Durner, W., Wessolek, G., 2011. Consistent parameter constraints for soil hydraulic functions. Advances in Water Resources 34, 1352–1365.

Piccinni, G., Ko, J., Marek, T., Howell, T., 2009. Determination of growth-stage-specific crop coefficients (K_c) of maize and sorghum. Agricultural Water Management 96, 1698–1704.

Portmann, F.T., Siebert, S., Döll, P., 2010. MIRCA2000— Global monthly irrigated and rainfed crop areas around the year 2000: a new high-resolution data set for agricultural and hydrological modeling. Global Biogeochemical Cycles 24 (1), GB1011.

Reynolds, W.D., Elrick, D.E., 2002. Pressure infiltrometer. In: Dane, J.H., Topp, G.C. (Eds.), Methods of Soil Analysis: Part 4, Physical Methods. SSSA Book Series No. 5. Soil Science Society of America, Madison, WI, pp. 826–836.

Ritchie, J.T., 1972. Model for predicting evaporation from a row crop with incomplete cover. Water Resources Research 8, 1204–1213.

Rockström, J., Falkenmark, M., Karlberg, L., Hoff, H., Rost, S., Gerten, D., 2009. Future water availability for global food production: the potential of green water for increasing resilience to global change. Water Resources Research 45 (7), W00A12.

Rockström, J., Folke, C., Gordon, L., Hatibu, N., Jewitt, G., Penning de Vries, F., Rwehumbiza, F., Sally, H., Savenije, H., Schulze, R., 2004. A watershed approach to upgrade rainfed agriculture in water scarce regions through Water System Innovations: an integrated research initiative on water for food and rural livelihoods in balance with ecosystem functions. Physics and Chemistry of the Earth, Parts A/B/C 29 (15–18), 1109–1118.

Rosegrant, M., Ximing, C., Cline, S., Nakagawa, N., 2002. The Role of Rainfed Agriculture in the Future of Global Food Production. EPTD Discussion Paper 90. International Food Policy Research Institute (IFPRI), Environment and Production Technology Division, Washington, DC http://www.ifpri.org/divs/eptd/dp/papers/eptdp90.pdf

Scanlon, B.R., Faunt, C.C., Longuevergne, L., Reedy, R.C., Alley, W.M., McGuire, V.L., McMahon, P.B., 2012. Groundwater depletion and sustainability of irrigation in the US High Plains and Central Valley. Proceedings of the National Academy of Sciences 109 (24), 9320–9325.

Schaap, M.G., Leij, F.J., 2000. Improved prediction of unsaturated hydraulic conductivity with the Mualem-van Genuchten model. Soil Science Society of America Journal 64, 843–851.

Schlenker, W., Roberts, M.J., 2006. Nonlinear effects of weather on corn yields. Applied Economic Perspectives and Policy 28 (3), 391–398.

Schuh, W.M., Cline, R.L., 1990. Effect of soil properties on unsaturated hydraulic conductivity pore-interaction factors. Soil Science Society of America Journal 54, 1509–1519.

Sharma, V., Irmak, S., 2012. Mapping spatially-interpolated precipitation, evapotranspiration and net irrigation requirements in Nebraska: Part II. Actual crop evapotranspiration and net irrigation requirements. Transactions of ASABE 55, 923–936.

Siebert, S., Döll, P., 2010. Quantifying blue and green virtual water contents in global crop production as well as potential production losses without irrigation. Journal of Hydrology 384 (3–4), 198–217.

Šimůnek, J., Sejna, M., Saito, H., Sakai, M., van Genuchten, Th.M., 2008. The HYDRUS-1D software package for simulating the one-dimensional movement of water, heat, and multiple solutes in variably saturated media. Version 4.0. HYDRUS Software Ser. 3. Dep. of Environ. Sci., Univ. of Calif., Riverside.

van Genuchten, Th, M., 1980. A closed form equation for predicting the hydraulic conductivity of unsaturated soils. Soil Science Society of America Journal 44, 892–898.

Wada, Y., van Beek, L.P.H.C., van Kempen, M., Reckman, J.W.T.M., Vasak, S., Bierkens, M.F.P., 2010. Global depletion of groundwater resources. Geophysical Research Letters 37 (20), L20402.